

# Dimple Fracture Simulation of Fracture Specimen under Different Constraint Conditions

Masanori Kikuchi<sup>1</sup>

**Abstract:** Three kinds of fracture specimens are tested under different constraint conditions. By the SEM (Scanning Electron Microscope) observation, it is shown that the roughness of fracture surface is different from each other largely. This is the effect of constraint condition. The dimple fracture process is simulated by the finite element method using Gurson's constitutive equation, and the crack tip stress fields are obtained. The distributions of stress triaxiality qualitatively agree with the experimental results. The J-R curves obtained also qualitatively agree with those of experiments, and the fracture surface roughness is well simulated.

**keyword:** Constraint effect, Dimple fracture, Void, FEM simulation, Gurson's constitutive equation

## 1 Introduction

In the elastic-plastic fracture mechanics, J integral concept [Rice(1968)] is considered to be one of the most important parameters, which controls the fracture process in the crack tip process zone. But by many experimental studies, it has been shown that the apparent J integral value changes due to the change of the constraint condition at the crack tip [Sorem, Dodds and Rolfe(1991); O'Dowd and Shih(1991)]. It is called constraint effect. Many studies have been conducted on the effect of the constraint [Anderson(1989), Dodds, Anderson and Kirk(1991)]. Practically, local approach [Beremin(1983); Mudry(1987), Xia and Shih(1996), Ruggieri and Dodds(1996), Koers, Krom and Bakker(1995)] gave one solution for the constraint condition problem. But the constraint condition on the microscopic fracture process has not been studied well yet. In this paper, constraint effect is studied experimentally by changing test conditions. They are; loading condition, initial crack length and specimen thick-

ness. The effects of the constraint condition on the microscopic fracture process and on the resistance curve are studied. Then the dimple fracture process is simulated numerically using Gurson's constitutive equation. Numerical results are compared with those of experiments, and the effect of the change of the constraint condition on the dimple fracture process is discussed.

## 2 Experiments

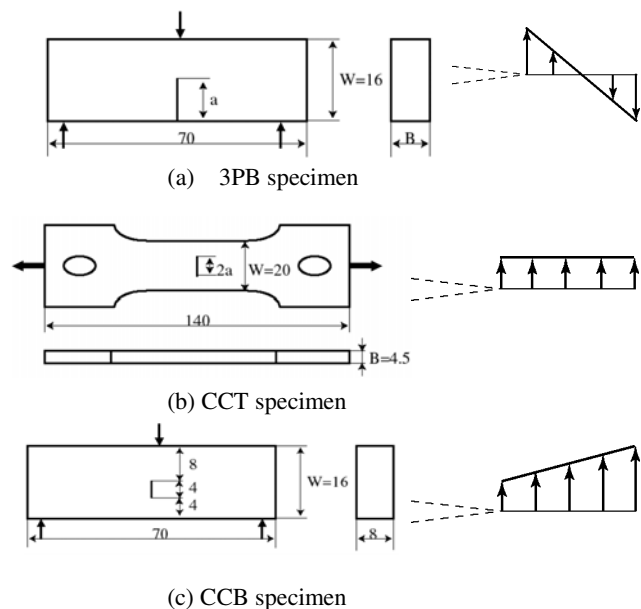


**Figure 1 :** Configurations of 3 kinds of specimens

Figure 1 shows the shape and size of three kinds of fracture specimen used in this study. They are ; (a) Three-Point-Bend Specimen (3PB), (b) Center Cracked Specimen in Tension (CCT) and (c) Center Cracked Specimen in Bending (CCB). CCB specimen has a crack inside of the specimen, and is subjected to three-point bending loading. It is designed for this experiment by author [Kikuchi and Nagai(1998)]. In each case, the stress field in the ligament of the specimen in the absence of crack

<sup>1</sup> Department of Mechanical Engineering, Faculty of Science and Technology, Tokyo University of Science, 2641, Yamazaki, Noda, Chiba, 278-8510, Japan

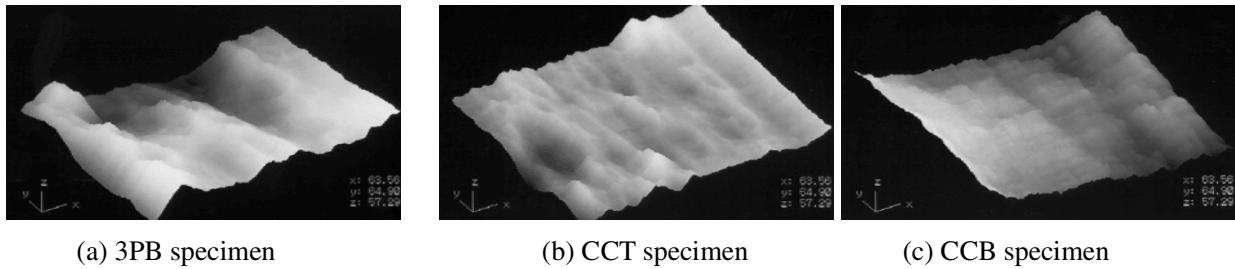


Figure 2 : Fracture surfaces of each specimen.

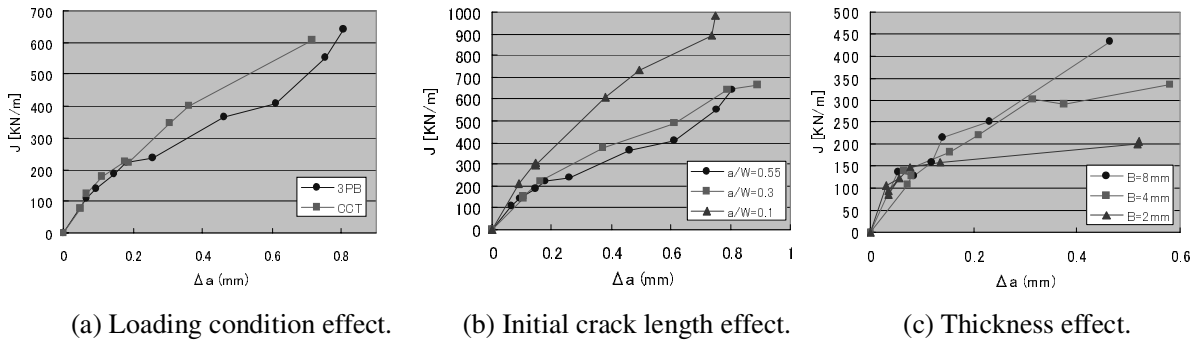


Figure 3 : J-R curves under different constraint condition.

Table 1 : Apparent  $J_{IC}$  value [kN/m]

3PB				CCT		
a/W	0.1	0.3	0.55	2a/W	0.4	0.6
B=2	306	175	151	B=4.5	185	186
B=4	339	239	165			
B=8	413	173	135			

tip changes one-by-one as shown in the right side of each specimen. For 3PB specimen, the stress is the largest at the crack tip and decreases gradually as the distance from the crack tip increases. In the CCT specimen, the stress keeps constant value, and in CCB specimen, stress increases as the distance from the crack tip increases. These different stress distribution patterns at the crack tip result the change of the constraint condition in the dimple fracture process.

The crack length and the thickness of 3PB specimen are changed to change the constraint condition at the crack tip. The crack length changes as  $a/W=0.1, 0.3$  and  $0.55$ , and the thickness,  $B$ , changes as  $B=2, 4$  and  $8\text{mm}$ . The crack length of CCT specimen is also changed in two cases,  $2a/W=0.4$  and  $0.6$ .

The material of the specimen is A533B steel, which is

used for the reactor pressure vessel. The fracture toughness is evaluated using 3PB and CCT specimens based on the JSME testing standard and using the conventional equations to evaluate  $J$  integral by the load-displacement record [JSME(1992)]. The results are shown in Table 1. As these values are not valid  $J_{IC}$  values, they are called apparent  $J_{IC}$ . The apparent  $J_{IC}$  values are strongly affected by the initial crack length of 3PB specimen. Generally speaking, it increases gradually as the initial crack length decreases. The apparent  $J_{IC}$  value also changes with the change of the thickness of 3PB specimen. But it does not show clear tendency. In CCT specimen, the initial crack length has not large effect on the apparent  $J_{IC}$  values. It is found that the specimen of  $B=8\text{mm}$  and  $a/W=0.55$  satisfies the size condition of the fracture toughness testing standard, and the valid  $J_{IC}$  value of this

material is determined as 135kN/m. All other apparent values are larger than this valid one. This is the effect of the constraint condition at the crack tip.

Figure 2 shows the SEM photos of the fracture surfaces of three specimens. They are the photos taken near the mid-plane of the specimen and near the initial crack tip. It is obvious that the surface roughness of each specimen is largely different from each other. In 3PB specimen, large dimples are observed and the roughness of the surface is the largest. In CCT specimen, the roughness becomes smaller than that of 3PB specimen. In CCB specimen, the fracture surface is smooth and large dimples disappear. The diameter of dimples is also measured using SEM photos, and it is found that many large dimples are observed in 3PB fracture surface, and in CCB specimen, there are few large dimples.

Figure 3-(a) shows J-R curves of 3PB( $a/W=0.55$ ,  $B=8\text{mm}$ ) and CCT specimens obtained experimentally. As the conventional equation for the J integral evaluation of CCB specimen does not exist, it cannot be evaluated experimentally. The J-R curve of 3PB specimen becomes smaller than CCT specimen as the crack grows. Constraint is stronger in 3PB specimen than in CCT specimen. It means that as the constraint becomes stronger, the J-R curve shows lower resistance curve. Figure 3-(b) shows J-R curves of 3PB specimens with different initial crack length ( $a/W=0.1, 0.3, 0.55$ ). As the initial crack length decreases, J integral value increases. Short initial crack length results weak constraint at the crack tip. This tendency agrees with that shown in Figure 3-(a). Figure 3-(c) shows J-R curves of 3PB specimens with different thickness ( $B=2\text{mm}, 4\text{mm}, 8\text{mm}$ ). As the thickness increases, J integral value decreases. Constraint becomes stronger for thicker specimen. This figures shows that as the constraint becomes stronger, J-R curve shows higher values, which is contrary to the former two figures. This is one important problem to be solved in this study.

The thickness effect appears in three-dimensional manner. Figures 4(a) and (b) show SEM photos of fracture surface for  $B=8\text{mm}$  and  $2\text{mm}$  specimens. They are photos at the mid-plane of each specimen. It is noticed that large dimples are observed in thick specimen, though they are not observed in thin specimen. In general, the dimple diameter value changes in wide range. Some are larger than  $100\mu\text{m}$ , and some are under  $1\mu\text{m}$ . In this study, larger voids, which are considered to be nucleated in the early stage of dimple fracture and have large effect

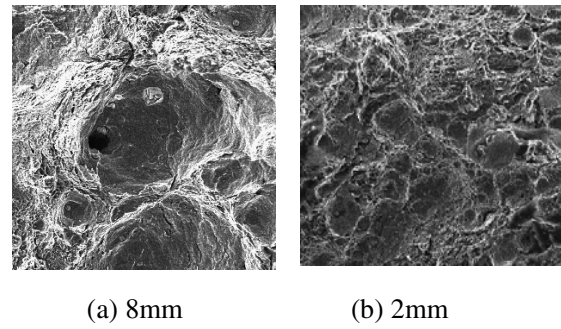


Figure 4 : Voids on Fracture surfaces (3PB)

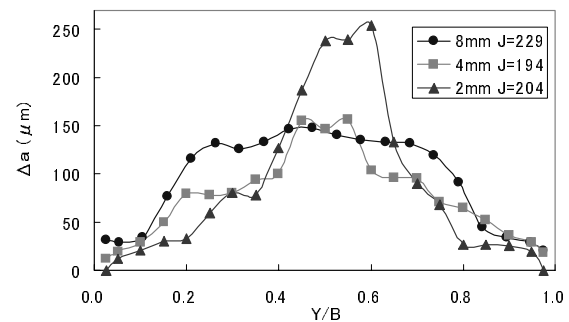


Figure 5 : Crack growth amount along the crack front.

on fracture process, are mainly considered. Number of voids larger than  $10\mu\text{m}$  is counted for three specimens, and the average diameter of them is shown in Table 2. The average dimple diameter changes with the specimen thickness. Thick specimen results large dimple diameter, and as the thickness decreases, it also decreases.

Table 2 : Average dimple diameter.

Thickness (mm)	8	4	2
Diameter ( $\mu\text{m}$ )	22.2	17.7	17.0

Figure 5 shows the crack growth patterns for three specimens. In this figure, the abscissa is the position along the crack front, which is normalized by the specimen thickness. Both sides ( $Y/B=0.0$  and  $1.0$ ) show specimen surfaces, and the center is the mid-plane of the specimen. The ordinate is the crack growth amount. In 8mm thick specimen, the crack growth occurs in wide area along the crack front. But in 2mm thick specimen, crack growth occurs mainly at the mid-part of the specimen. As a result, the crack front configuration becomes steep in thin specimen. In 2mm thick specimen, the fracture mode at

specimen surface is shear type fracture, and shear-lip is observed.

Through these experiments, it is shown that constraint condition affects the microscopic fracture process, such as void nucleation and growth largely. It is also shown that it has large effects on macroscopic parameter, J-R curve. The mechanism of these effects is studied by numerical simulation.

### 3 FEM Analysis

#### 3.1 Gurson's constitutive equation

To consider the microscopic fracture process, the simulation of the nucleation, growth and coalescence of voids is needed. For this purpose, FEM analysis using constitutive equation proposed by Gurson [Gurson(1970)] and later modified by Tvergaard [Tvergaard(1982)] is conducted. This constitutive equation is shown as follows.

$$\Phi = \frac{3}{2} \frac{\sigma'_{ij}\sigma'_{ij}}{\bar{\sigma}_m^2} + 2f^* q_1 \cosh\left(\frac{q_2 \sigma_{kk}}{2\bar{\sigma}_m}\right) - (1 + q_1^2 f^{*2}) \quad (1)$$

where  $\sigma'_{ij}$  is the deviatoric stress,  $\bar{\sigma}_m$  is the equivalent stress,  $f^*$  is the void volume fraction and  $q_1, q_2$  are constants proposed by Tvergaard. The function  $f^*$  is shown as follows.

$$f^* = \begin{cases} f & f \leq f_c \\ f_c + \frac{f_u - f_c}{f_F - f_c} (f - f_c) & f \geq f_c \end{cases} \quad (2)$$

Where  $f$  is the void volume fraction,  $f_u^*$  is  $1/q_1$ ,  $f_c$  is the critical void volume fraction,  $f_F$  is the void volume fraction when the material loses all stress carrying capacity. The rate of increase of void volume fraction is shown as follows.

$$\dot{f} = (1 - f)\dot{\epsilon}_{kk}^p + A(\dot{\bar{\sigma}}_m + \dot{\sigma}_{kk}/3) + B\dot{\bar{\epsilon}}_m^p \quad (3)$$

The first term in equation (3) accounts for the growth of existing voids, the second term models the nucleation of voids by a stress controlled mechanism, while the third term corresponds to plastic strain controlled void nucleation. In this paper, plastic strain controlled nucleation is considered, and A and B in eq.(3) are given as follows [Chu and Needleman(1980)].

$$A = 0, \quad B = \frac{f_N}{S_N \sqrt{2\pi}} \exp\left[-\frac{1}{2} \left(\frac{\bar{\epsilon}^p - \epsilon_N}{S_N}\right)^2\right] \quad (4)$$

where  $f_N$  is volume fraction of void nucleating particles,  $S_N$  is the corresponding standard deviation,  $\epsilon_N$  is the mean strain for nucleation.

**Table 3** : Material properties (A533B steel)

Young's modulus	E	206[GPa]
Poisson's ratio	$\nu$	0.3
Initial yield stress	$\sigma_{ys}$	599[GPa]
Critical void volume fraction	$f_c$	0.133
Void volume fraction at final	$f_F$	0.188
Volume fraction of void nucleating particles	$f_N$	0.02
Standard deviation of void nucleation	$S_N$	0.1
Mean strain for void nucleation	$\epsilon_N$	0.3

As many parameters are needed for the use of Gurson's model, they are determined based on literature [Broek(1973)] and by authors' study [Kikuchi, Miyamoto, Ootoyo and Kuroda(1990)] as shown in Table 3. It is also pointed out that the numerical results using Gurson's model depends largely on the element size. Then in the following numerical simulation, the mesh size around the crack tip zone is kept to be same for every numerical model. Quantitatively, a little different result may be obtained if we use another mesh size. In this study, qualitative evaluation is mainly conducted. Quantitative evaluation is not done because both two-dimensional and three-dimensional models are used in the following. For the use of Gurson's model, the finite deformation analysis is needed. For this purpose, crossed triangle element and super-box element are used for 2-dimensional and 3-dimensional models, respectively, in FEM modeling.

#### 3.2 Effect of loading condition

Two dimensional plane strain analyses are conducted for three kinds of specimens shown in Figure 1. For 3PB specimen, crack length,  $a/W$  is assumed to be 0.55. Figure 6 shows one example of the mesh pattern of 3PB specimen. The crack tip is modeled as a notch to simulate the blunting of the crack tip. For CCT and CCB specimen, same mesh patterns are used near the crack tip area.

In the real material, many particles are distributed randomly in the material. They are segregated particles or

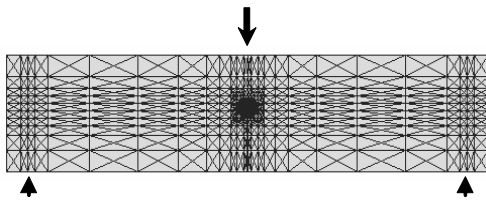


Figure 6 : Mesh pattern of 3PB specimen.

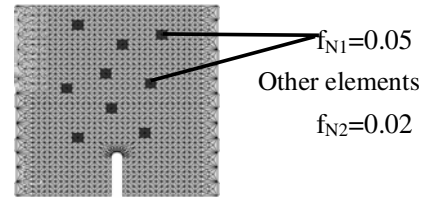
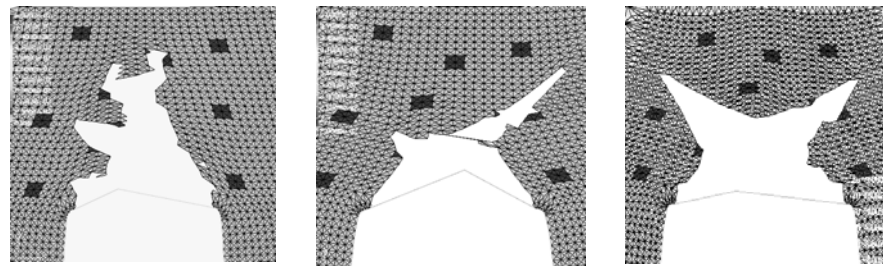
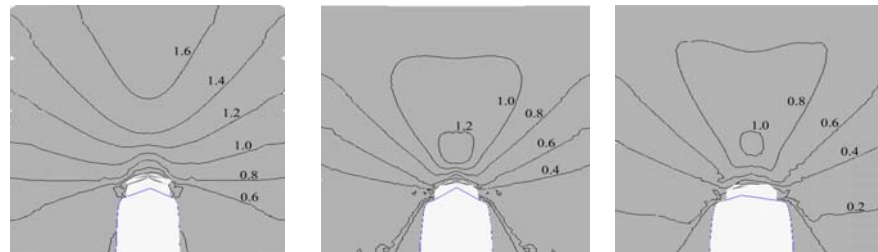


Figure 7 : Mesh pattern around the crack tip



(a) 3PB specimen (b) CCT specimen (c) CCB specimen

Figure 8 : Fracture pattern (Different loading condition)



(a) 3PB specimen (b) CCT specimen (c) CCB specimen

Figure 9 : Distribution of stress triaxiality (Different loading condition)

inhomogeneous particles. It is considered that the dimple fracture occurs by connecting large voids originating from larger particles, and this mechanism affects roughness of fracture surface. For the simulation of such inhomogeneous structure of the material, inclusions are assumed around the crack tip as shown in Figure 7. The black marks model the large particles where the initial volume fraction of inclusions ( $f_N$ ) is assumed to be larger ( $f_{N1}=0.05$ ) than other areas ( $f_{N2}=0.02$ ).

The fracture processes of this model are shown in Figure 8 (a)-(c). The crack growth of 3PB specimen is affected by the existence of particles, and crack growth occurs by connecting large particle areas. The fracture of CCT specimen grows rather straight, and the effect of particles is not clear. In CCB specimen, the fracture is not affected by the existence of large particles. Comparing these three figures, it is noticed that the roughness of the

fracture surface is largely different from each specimen. In 3PB specimen, rough fracture surface is generated, though smooth surfaces are observed in other two specimens. These results agree with SEM photos in Figure 2 qualitatively.

Figure 9 (a)-(c) shows the distribution of stress triaxiality at the beginning of the dimple fracture around the crack tip for three specimens. Stress triaxiality is deeply related with the nucleation and growth of voids. In 3PB specimen, high stress triaxiality area exists in wide area around the crack tip.

But in CCT specimen, high stress triaxiality area becomes narrow. In CCB specimen, there is little high stress triaxiality area around the crack tip.

In 3PB specimen, high stress triaxiality area spreads widely around the crack tip. If this area is large, many

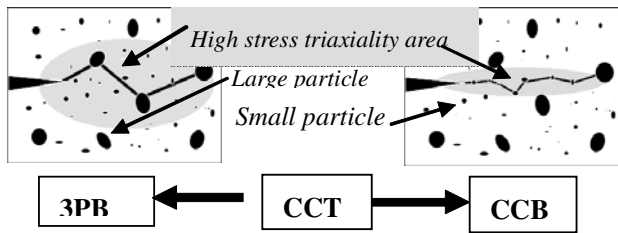


Figure 10 : Dimple fracture process.

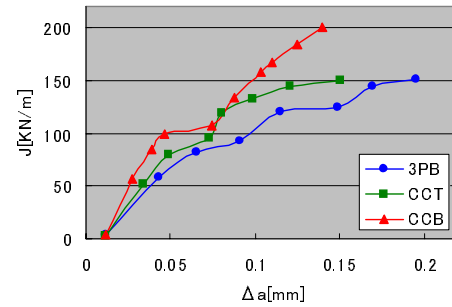


Figure 11 : J-R curves.

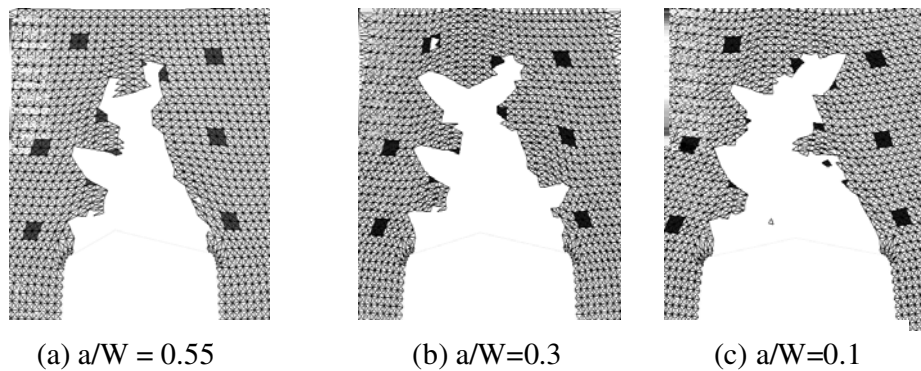


Figure 12 : Fracture pattern for different crack length

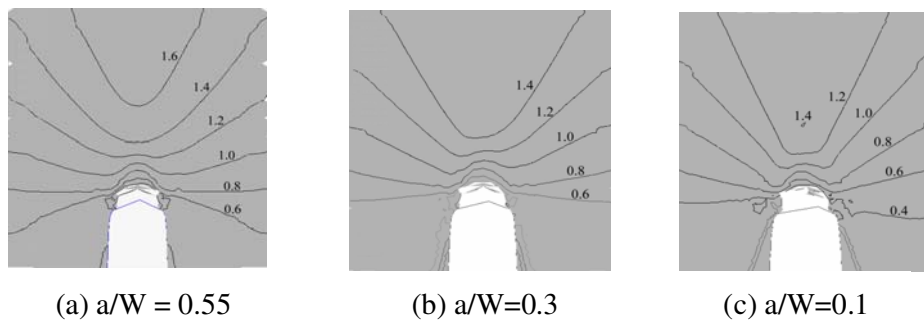


Figure 13 : Distribution of stress triaxiality

large particles are included in this area, and large voids are nucleated easily. By connecting them, rough fracture surface is created as shown in Figure 10.

In CCT and CCB specimen, high stress triaxiality area is narrow. In these specimens, final fracture occurs by connecting small voids nucleated at small particles. It generates rather smooth surface. It is shown that the effect of the loading on the fracture surface roughness is well simulated by these numerical analyses.

Figure 11 shows the relation between J integral value and the crack growth amount. In the experiment, this rela-

tion is called J-R curve. It is interesting to notice that by the numerical simulation, the relation between J and  $\Delta a$  shows nearly bi-linear relation. The first straight line is similar to the blunting line in the experiment, and the second line is corresponding to the resistance curve. This figure shows that the resistance is lower for stronger constraint specimen, and it increases as the constraint condition becomes weak. By comparing this figure with Fig.3-(a), it is obvious that both results are similar to each other qualitatively very well. When the constraint is strong at the crack tip, voids are nucleated easier due to the high

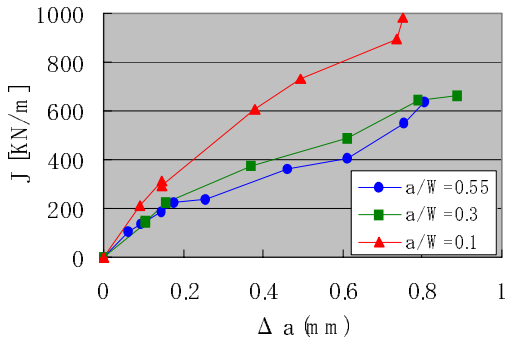


**Figure 14 :** J-R curves for different initial crack length 3PB specimens.

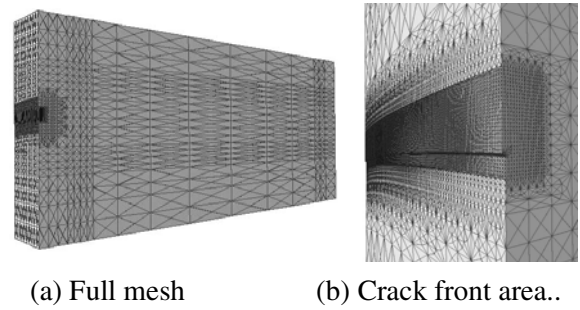
stress triaxiality zone. Then the crack growth may occur with small resistance. This is the reason of the tendency of Figure 3-(a) and Figure 11.

### 3.3 Effect of Initial Crack Length

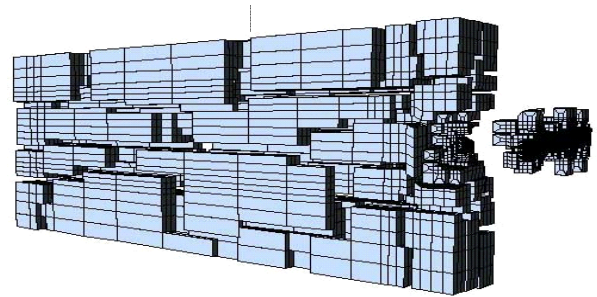
Effect of the different initial crack length of 3PB specimen is studied using same method of the previous section. The initial crack length is changed as  $a/W=0.1, 0.3, 0.55$ . The final fracture patterns are shown in Figure 12 (a)-(c). At first, the fracture occurs perpendicular to the original crack growth direction, and it changes the direction to the initial crack direction after some amount of crack growth. The amount of the crack growth perpendicular to the initial crack direction increases as the initial crack length decreases. Except this point, all specimens show similar fracture process, and are affected by the existence of large particles.

Figure 13(a)-(c) shows the distribution of stress triaxiality around the crack tip for three specimens at the beginning of the dimple fracture. In  $a/W=0.55$ , high stress triaxiality area exists in wide area ahead of the crack tip. But in  $a/W=0.3$ , high stress triaxiality area becomes narrow. In  $a/W=0.1$ , there is little high stress triaxiality area around the crack tip.

Figure 14 shows J-R curves for these three specimens. Specimen with the shortest crack gives the highest resistance value, and that with the longest crack gives the lowest resistance. It also agrees with the experimental results shown in Fig.3-(b). Also it is noticed that the strong constraint results lower resistance curve, which agrees with the results of the effect of the loading condition, shown in section 3.2.



**Figure 15 :** Mesh pattern of 8mm thick specimen



**Figure 16 :** Domain Decomposition for Parallel computing.

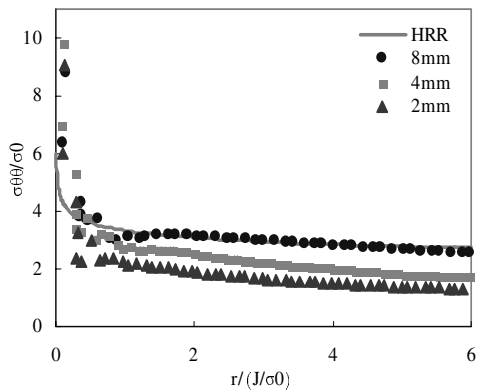
### 3.4 Effect of Specimen Thickness

Fig.15(a) shows the mesh pattern of the 8mm thick specimen. Fig.15(b) is a mesh pattern around the crack front. As the initial crack introduced by fatigue pre-cracking has some curvature, the crack front is modeled by measuring the real crack front configuration experimentally. The total number of elements and number of nodes for each model are shown in Table 4.

**Table 4 :** Mesh size

	Nodes	Elements
8mm	474028	92900
4mm	247298	48230
2mm	134568	26020

As large number of nodes is used in modeling, single CPU is not enough to solve this problem. Parallel computing technique [Yagawa and Shioya(1993)] is employed, and 8 PC Cluster is used. Figure 16 shows one example of mesh decomposition for parallel computing. One model is decomposed in more than 50 domains, and in each CPU, nearly 6 domains are processed.



**Figure 17 :** Crack tip stress fields at the mid-plane of the specimen.

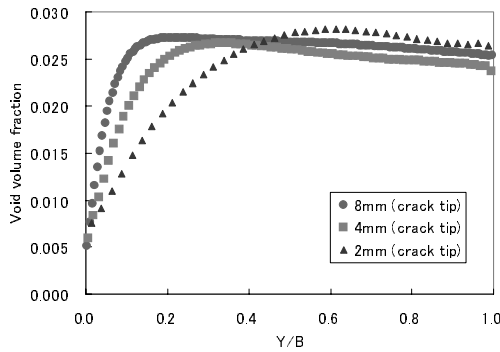


**Figure 19 :** Void volume fraction distribution

By the plane strain fracture toughness testing standard, the specimen thickness is defined to satisfy following equation.

$$B \geq 25 \frac{J_{in}}{\sigma_{fs}} \quad (5)$$

where B is the specimen thickness,  $J_{in}$  is the J value for crack growth initiation, and  $\sigma_{fs}$  is flow stress.

When  $J_{in}$  value satisfies this equation, it becomes valid fracture toughness value,  $J_{IC}$ . For A533B specimen, used in this study, the minimum thickness of the specimen is 7.0mm. In this study, 4mm and 2mm thick specimens are used. They don't satisfy this condition.

The crack tip stress fields of these specimens are compared with HRR fields [Hutchinson(1968), Rice and Rosengren(1968)]. Figure 17 shows the crack tip stress fields for three specimens at the mid-plane of the specimen. For 8mm thick specimen, which satisfies equation (5), the stress field agrees well with HRR solution. It means that the J integral is a dominant parameter for the

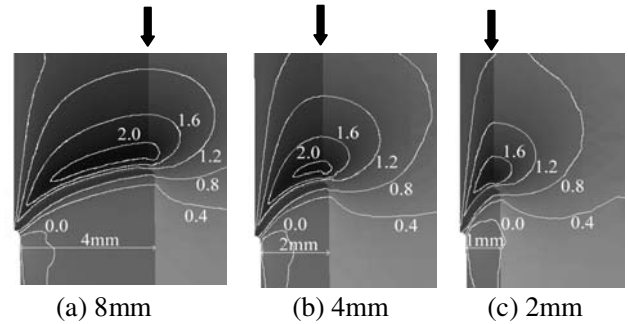


**Figure 18 :** Stress triaxiality distributions around the crack tip.

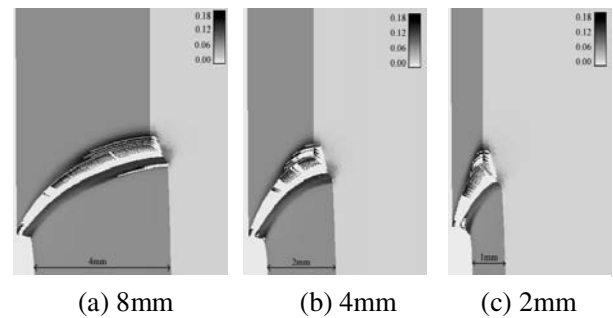


**Figure 20 :** Crack growth patterns for three specimens.

crack tip stress field of this specimen. But for other 2 specimens, the crack tip stress fields deviate from HRR field. When the crack tips stress field is lower than HRR field, it means that the constraint is weak at the crack tip. Figure 17 shows the constraint becomes weak as the specimen thickness becomes small.

Figure18 shows the distributions of stress triaxiality around the crack tip for three specimens. These figures show a quarter of each specimen. The left side is the surface of the specimen, and a line indicated by an arrow is the mid-plane of the specimen. Right side from this arrow-line is a cross section of the mid-plane of the specimen. These are just after the dimple fracture initiation at the mid-plane of the specimen. In Figure 18(a), which is a result of thick specimen, a high stress triaxiality area spreads inside of the specimen widely. As the thickness decreases, high stress triaxiality area decreases and the highest value also decreases with it. Stress triaxiality affects largely on the nucleation and growth of void, which plays main role in dimple fracture. These fig-

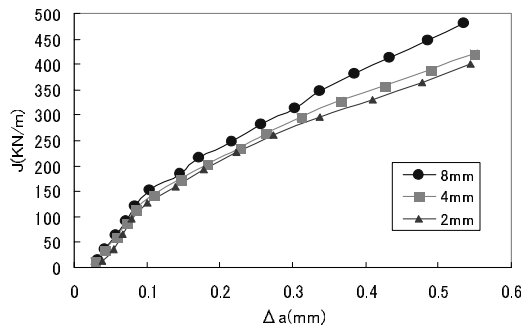


Figure 21 : J-R curves of three specimens

ures are deeply related with experimental results shown in Fig.4, where large voids are observed in thick specimen and voids become small in thin specimen.

Fig.19 shows the distribution of void volume fraction along the crack front for three specimens. In this figure, the abscissa is the position along the crack front, normalized by the specimen thickness.  $Y/B=0.0$  means the specimen surface, and 1.0 is the mid-plane of the specimen. Results are similar to those of stress triaxiality distributions. For thick specimen, high void volume fraction area is widely spread in the specimen thickness direction, though it is narrow in thin specimen. It also agrees qualitatively with the experimental observation.

Figure 20 shows crack growth patterns for three specimens. These figures are the results when J value is nearly 200kN/m, after large amount of dimple fracture growth. In these figures, white zones in front of initial crack front mean the dimple fracture areas. The location of the cross section of each specimen is the same as that in Figure 18. It is shown that these results are deeply related with those of Figure18 and Figure19. Dimple fracture occurs in wide area in 8mm thick specimen. But in 2mm thick specimen, dimple fracture occurs only at the mid-plane, and steep crack front configuration is generated. In this simulation, shear lip type fracture process is not considered. In the real specimen, shear lip fracture occurs in 2mm thick specimen at both crack edges. But finally, the crack growth amount is the largest at the mid-plane of the specimen, which quantitatively agrees with these numerical simulations.

Fig.21 shows J-R curves obtained by numerical simula-

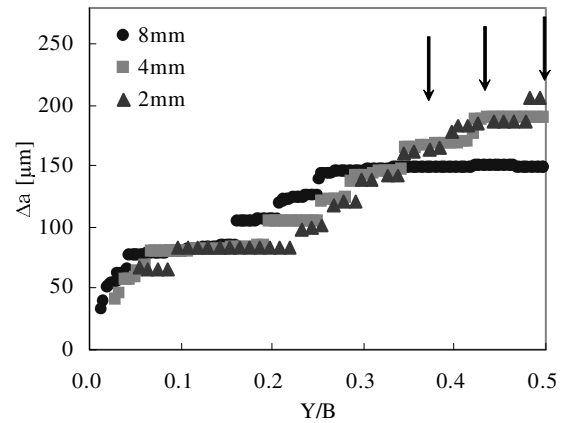


Figure 22 : Fracture pattern along the crack tip.

tion. The ordinate, J integral value, is evaluated using conventional equation using the load-displacement data obtained numerically. The line integration is also conducted. But after some amount of crack growth, plastic zone spreads widely, and J integration path crosses with the plastic zone. Then valid J value is not obtained by line integration. The abscissa is crack growth amount. It is determined as the average value measured at 5 points along the crack front, due to the fracture toughness testing standard. Similar to experimental result, Fig.3, J-R curve of thick specimen is higher than that of thin specimen. In my previous paper [Kikuchi and Sasaki (2002)], the J-R curve becomes high for low-constraint condition, and low J-R curve is obtained for high constraint condition. In this study, thick specimen is under high constraint condition and thin specimen is under low constraint condition. But the results show that high constraint condition specimen results high J-R curve. It is contrary to the previous paper.

The reason of this tendency is due to the method to determine the crack growth amount experimentally. By the fracture toughness standard, the crack growth amount is defined as the average of 5 points along the crack front. These 5 points are near the mid-plane of the specimen. Figure 22 shows fracture patterns of three 3PB specimens, obtained numerically. The abscissa is the half of the specimen thickness, where  $Y/B=0.0$  is the specimen surface and  $Y/B=1.0$  is the mid-plane of the specimen. In this figure, locations of 3 points to measure the crack growth amount are shown by arrows. As shown in this figure, the distribution patterns of crack growth amount at these locations are largely different from each other

in three specimens. In thick specimen, crack growth amount is nearly constant along the crack front, but it changes largely in thin specimen. By this reason, the average crack growth amount of thin specimen becomes larger than that of thick specimen. This is the main reason of the difference of J-R curves due to the difference of the specimen thickness.

#### 4 Concluding Remarks

By the experimental studies, it is shown that the constraint effects appear in the apparent  $J_{IC}$  value and J-R curves of three kinds of specimens. They are macroscopic parameters on the fracture process. By the numerical simulation, microscopic fracture process is studied, and the effect of constrain condition is shown. It became obvious that the microscopic fracture process is largely affected by the change of the constraint condition, which results the change of the macroscopic fracture parameters. Following results are obtained.

The change of the roughness of the fracture surface due to the change of the constraint condition is related with the stress triaxiality distribution around the crack tip.

The reason that the weak constraint condition results higher J-R curve is understood well by the stress triaxiality distribution at the crack tip.

The thickness effect is well explained by this numerical simulation.

Finally, it should be pointed out that the thickness effect is deeply related with the shear lip fracture near the free surface, under the plane stress condition. Dimple fracture simulation using Gurson's constitutive equation assumes plane strain condition. Thickness effect should be studied with the consideration of the shear lip fracture at the surface of the specimen, which is a future target of my study.

#### References

- Anderson, T. L.**(1989), "Crack tip parameters for large scale yielding and low constraint configurations", *Int. J. Fracture* 41, pp.79-104
- Beremin, F.M.** (1983); A Local Criterion for Cleavage Fracture of a Nuclear Pressure Vessel Steel, *Metallurgical Transactions*, 14A, pp.2277-2287
- Broek, D.**(1973); The role of inclusions in ductile fracture and fracture toughness, *Eng. Frac. Mech.*, vol.5, pp.55-56
- Chu, C. and Needleman, A.** (1980): Void nucleation effects in biaxially stretched sheets, *Trans. ASME, J. Engng. Mater. Tech.*, 102,pp.249-256
- Dodds, R.H.; Anderson, T.L.; Kirk, M.T.**(1991); A framework to correlate a/W ratio effects on elastic-plastic fracture toughness ( $J_c$ ), *Int. J. Fracture*, vol.48, pp.1-22
- Gurson, A.L.**(1977); Continuum Theory of Ductile Rupture by Void Nucleation and Growth: Part I - Yield Criteria and Flow Rules for Porous Ductile Media, *Trans. ASME, J. Engineering and Materials and Technology*, 99, pp.2-15
- Hutchinson, J.W.** (1968): Singular Behavior at the End of a Tensile Crack in a Hardening Materials, *J. Mech. Phys. Solids*, vol.16, pp.13-31
- JSME Standard S 001-1992** (1992), Standard Method of Test for Elastic-Plastic Fracture Toughness  $J_{IC}$ (Supplement, 1<sup>st</sup> Edition), *Japan Society of Mechanical Engineers*
- Kikuchi, M , Miyamoto, H. , Otoyoy, H and Kuroda, M** (1991); Ductile Fracture of Aluminum Alloys (Observation of the Fracture Process by FRASTA and FEM Simulation) *JSME International Journal Series I, Vol.34 , No.1*, pp.90-97
- Kikuchi, M. and Nagai, M.** (1998): Constraint Effect at the Crack Tip (2<sup>nd</sup> Report: Constraint Effect of High Toughness Material), *Trans. JSME(in Japanese), Ser.A*, 64-625, pp.2367-2373
- Kikuchi, M. and Sasaki, J.**(2003): Dimple Fracture Simulation under the Different Constraint Condition, *Trans. JSME(in Japanese), Ser.A*, 69-687, pp.1621-1627
- Koers R. W. J., Kroom A. H. M. and Bakker A.** (1995): "Prediction of Cleavage Fracture in the Brittle to Ductile Transition Region of a Ferric Steel, Constraint Effects in Fracture Theory and Applications", *ASTM STP 1224*, pp.191-208.
- Murdy, F** (1987); A Local Approach to Cleavage Fracture, *Nuclear Engineering and Design*, vol.105, pp.65-76
- O'Dowd N. P and Shih C. F.**(1991), "Family of crack-tip fields characterized by a triaxiality parameter-I. Structure of fields", *J. Mech. Phys. Solids* 39, pp.989-1015
- Rice, J.R.** (1968); A Path Independent Integral and the Approximate Analysis of Strain Concentration by Notches and Cracks, *Transactions. ASME, J. Applied Mechanics*, vol.90, Series E, pp.379-386

**Rice, J.R. and Rosengren, G.F.**(1968): Plane Strain Deformation near a Crack Tip in a Power-Law Hardening Material, *J. Mech. Phys. Solids*, vol.16, pp.1-12

**Ruggieri C. and Dodds Jr.**(1996), “A transferability model for brittle fracture including constraint and ductile tearing effects: a probabilistic approach”, *Int. J. Fracture* 79, pp.309-340.

**Yagawa G. and Shioya R.** (1993), “Parallel finite elements on a massively parallel computer with domain decomposition”, *Comput. Systems Eng.*, 4 pp.495-503

**Sorem. W. A., Dodds. R. H. and Rolfe. S. T.**(1991): “Effects of crack depth on elastic-plastic fracture toughness”, *Int. J. Fracture* 47, pp.105-126

**Tvergaard. V.**(1982): “On localization in ductile materials containing spherical voids”, *Int. J. Fracture* 18, pp.237-252

**Xia L. and Shih C. F.** (1996): “Ductile crack growth-III. Transition to cleavage fracture incorporating statistics”, *J. Mech. Phys. Solids* 44, pp.603-639

